minerals

MDPI

Article

Antigorite Dehydration under Compression and Shear Loadings in a Rotational Diamond Anvil Cell

Dayong Tan [1,2,*,†], Changguo Jiang [2,3,4,†], Weishan Chen [2,3,4], Yi Tan [2,3,4], Binbin Yue [5] and Wansheng Xiao [2,3,*]

1 Institute of Advanced Science Facilities, Shenzhen 518107, China
2 Key Laboratory of Mineralogy and Metallogeny, Guangzhou Institute of Geochemistry, Chinese Academy of Sciences, Guangzhou 510640, China
3 Key Lab of Guangdong Province for Mineral Physics and Materials, Guangzhou 510640, China
4 University of Chinese Academy of Sciences, Beijing 100049, China
5 Center for High Pressure Science & Technology Advanced Research, Beijing 100094, China
* Correspondence: tandayong@mail.iasf.ac.cn (D.T.); wsxiao@gig.ac.cn (W.X.)
† These authors contributed equally to this work.

Abstract: Mineral dehydration in the subduction zone enormously affects Earth's geodynamics and the global geochemical cycles of elements. This work uses Raman spectroscopy and X-ray diffraction to investigate the dehydration process of antigorite under compression and shear loading conditions in a rotational diamond anvil cell (RDAC) at room temperature. In order to compare the shear effects, T301 stainless steel and Kapton plastic are applied as the gasket materials. In the experiment using a high-strength T301 stainless steel gasket, two new broad OH-stretching peaks of H_2O and $H_3O_2^-$ appear at 3303 and 3558 cm^{-1}, respectively, at 1.7 GPa. The original sharp OH-stretching peaks of antigorite at 3668 and 3699 cm^{-1} remain, while the central pressure is increased to 8.0 GPa, and the largest pressure gradient is about 2.5 GPa in the sample chamber. In another experiment with a low-strength gasket of Kapton plastic, two new OH-stretching broad peaks of H_2O and $H_3O_2^-$ also start to appear at 3303 and 3558 cm^{-1}, respectively, at a lower pressure of 0.3 GPa, but the original sharp OH-stretching peaks of antigorite at 3668 and 3699 cm^{-1} almost completely vanish as the central pressure reaches 3.0 GPa, with the largest pressure gradient at around 4.8 GPa. The comparison between the two experiments shows that antigorite is easier to dehydrate in the chamber of a Kapton plastic gasket with a larger gradient of shear stress. However, its axial compression stress is lower. The high-pressure Raman spectra of $MgO_2(OH)_4$ octahedron and SiO_4 tetrahedron in the low wavenumber zones (100–1200 cm^{-1}) combined with the micro-beam X-ray diffraction spectrum of the recovered product strongly support the structural breakdown of antigorite. This investigation reveals that the water-bearing silicate minerals have strong shear dehydration in the cold subduction zone of the plate, which has important applications in predicting the physical and chemical properties of subduction zones and deducing the rate of plate subduction.

Keywords: antigorite; rotational diamond anvil cell; shear stress; dehydration; Raman spectroscopy

check for updates

Citation: Tan, D.; Jiang, C.; Chen, W.; Tan, Y.; Yue, B.; Xiao, W. Antigorite Dehydration under Compression and Shear Loadings in a Rotational Diamond Anvil Cell. *Minerals* **2023**, *13*, 871. https://doi.org/10.3390/min13070871

Academic Editor: Jordi Ibanez-Insa

Received: 16 June 2023
Revised: 24 June 2023
Accepted: 26 June 2023
Published: 28 June 2023

Copyright: © 2023 by the authors. Licensee MDPI, Basel, Switzerland. This article is an open access article distributed under the terms and conditions of the Creative Commons Attribution (CC BY) license (https://creativecommons.org/licenses/by/4.0/).

1. Introduction

Mineral dehydration in Earth's interior is associated with various geological activities, major geological events, and livable environments. Mineral dehydration produces numerous H^+ protons or $H_3O_2^-$ hydrated hydroxyls, which significantly change the oxidation/reduction state of mantle rocks, enhance the mobility and conductivity of particles, and ultimately promote material circulation and energy transmission in mantle convection.

Serpentine group minerals are the main hydrous phase in oceanic plates and are the most abundant water-bearing mineral in altered ultramafic rocks with water content up to ~13 wt% [1–4]. The dehydration of serpentine is thought to contribute to the generation of arc magmatism, and of intermediate and deep earthquakes. There are four main forms of serpentine: chrysotile, lizardite, antigorite, and polygonal serpentine, which are

characterized by a layered structure and where sheets of SiO_4 tetrahedra alternate along the c direction with sheets of $MgO_2(OH)_4$ octahedra [5,6]. In antigorite, the high-pressure, high-temperature monoclinic form of serpentine, the layers show a pronounced curvature along the basal plane, which is accompanied by changes in the polarity of the tetrahedral layer [7,8]. The dehydration reaction of antigorite has been widely carried out at high pressure and temperature conditions to detect dehydration behavior.

The high pressure and room temperature experiment shows that no amorphization, phase transition, or hysteresis will occur in antigorite during compression to 10 GPa, and that no decompression to ambient pressure will occur at hydrostatic pressure conditions [9,10]. Pressure-induced amorphization of serpentine has been observed at temperatures of 200 to 300 °C and pressures of 14 to 27 GPa with a combination of a multi-anvil apparatus and synchrotron radiation. The high-pressure phases then crystallized rapidly when the temperature was increased to 400 °C [11]. In the range of 350–710 °C and 0.2–5.0 GPa in a standard cold-seal hydrothermal pressure vessel and an end-loaded piston-cylinder apparatus, the high-temperature and pressure experiments exhibit that the m value of natural antigorite ($Mg_{3m-3}Si_{2m}O_{5m}(OH)_{4m-6}$) changes systematically with pressure and temperature, and that small amounts of free fluid are liberated [12]. The piston-cylinder experiments from 600–650 °C and 2.5–4.5 GPa also show that natural antigorite produced small amounts of fluid during prograde subduction zone conditions [13]. At 630–660 °C and pressures greater than 1.6 GPa, antigorite first reacts with talc to form orthopyroxene ± chlorite and fluid [14]. The deformation experiments of antigorite at 1100–1500 MPa and 400–600 °C using a solid-medium Griggs-type apparatus revealed that antigorite samples decomposed to forsterite and enstatite under shear stress at temperatures ≥550 °C but remained in their original phase under triaxial compression at 600 °C [2]. Using a Tuttle-type autoclave, the dehydration kinetics experiments at 200 MPa and 500–600 °C showed the dehydration reaction of antigorite to form forsterite and that talc has a heterogeneous nucleation and growth mechanism [4]. Previous high-pressure studies have shown that high temperature is a key factor for antigorite dehydration.

However, in the early ocean–ocean subduction, ocean–continent subduction, and land–continent subduction, a cold subduction slab exists. The structural stability of hydrous minerals in these cold subducting slabs mainly depends on their subducting depth (axial compression stress) and moving speed (horizontal shear stress). Furthermore, with regard to the depth and/or moving speed, what really dominates the mineral dehydration within the cold subducting slabs? In order to detect the dehydration behavior at ambient temperature and compression–shear circumstances, we applied a rotational diamond anvil cell (RDAC) device [15,16], which is a very useful tool to provide the compression–shear stress and to carry out in-situ Raman measurements of the natural antigorite samples with different strength gasket materials.

2. Materials and Methods

Natural antigorite was obtained from the Xiuyan County of Liaoning Province in Northeast China, which is a well-known Serpentine-rich area in China. The antigorite fragments were grounded with an agate pestle and mortar to <50 μm. The Raman and X-ray powder diffraction spectra show that the white powder sample was a typical antigorite $Mg_3(Si_2O_5)(OH)_4$ with a characteristic lattice; silicate layer internal vibrational modes at 228, 375, 458, 635, 686, 1045 cm^{-1}; and OH stretching vibrations at 3668 and 3699 cm^{-1}, corresponding to a monoclinic structure (space group: C2/m, a = 5.424 Å, b = 9.238 Å, c = 7.274 Å, and β = 91.32°). These data are consistent with previously reported values [4,8].

Raman microscopy of the sample and diamond was measured at the focal plane using a confocal Renishaw 2000 instrument, equipped with two monochromator gratings and a charge coupled device detector (CCD) as well as a Leica optical microscope with an objective of long-focus ×20. An 1800 g/mm grating and 100 μm aperture resulted in a 1 cm^{-1} spectral resolution. The 532.4 nm line of the Nd:YVO_4 laser was used as the incident light source. The transparent sample in the RDAC was observed to be insensitive

to laser radiation. Therefore, the laser power is not limited during the high-pressure Raman measurements. The laser power reaching the sample in this system is about 1 mW. The laser spot on the sample and diamond was about 2 μm in diameter and 1 μm in depth. Raman spectra were acquired in the 100–1200 cm^{-1} and 2750–5000 cm^{-1} spectral ranges. The acquisition time was 20 s, averaging over three accumulations per spot.

X-ray diffraction (XRD) patterns of the sample were recorded by a Rigaku D-max Rapid-V micro-diffractometer (μ-XRD), which was equipped with a microfocus rotating anode source (MicroMax-007HFM X-ray generator, Rigaku, Tokyo, Japan) and a curved imaging plate detector. The working voltage and current of CuKα were 40 kV and 30 mA. The diameter of the collimator was 0.1 mm, and the collection time was 300 s. The two-dimensional images collected by the built-in CCD were converted into diffraction angle and intensity data by Rigaku 2DP software (Rigaku, Tokyo, Japan).

The compression and shear loading experiments were carried out in a rotational diamond anvil cell (RDAC) at room temperature (Figure 1). The RDAC consists of two cylinders and a piston with a pair of diamonds of 500 μm diameter culets. In order to obtain the different shear effects, we selected T301 stainless steel and Kapton plastic as the gaskets, two typical gaskets with completely distinct strengths. The sample chambers had the same 400 μm diameters. In the compression and shear loading experiments, the samples were firstly compressed by turning the screw to close the diamonds, which were located in the cylinder and piston. Then the shear stress was loaded into the compressed sample by rotating the inner piston. In the T301 stainless steel gasket experiment, the sample was compressed gradually to central pressures of 5.0 and 8.0 GPa and rotated in a 45° step to 360° at both pressure points. The pressure and Raman spectra of 17 points in the sample chamber were measured during compression and rotation. In the Kapton plastic gasket experiment, the sample was compressed gradually to central pressures of 1.3, 3.0 and 4.5 GPa, and further rotated in a 45° or 90° step to 360° at these pressure points. The pressure and Raman spectra of 21 points in the sample chamber were measured during compression and rotation.

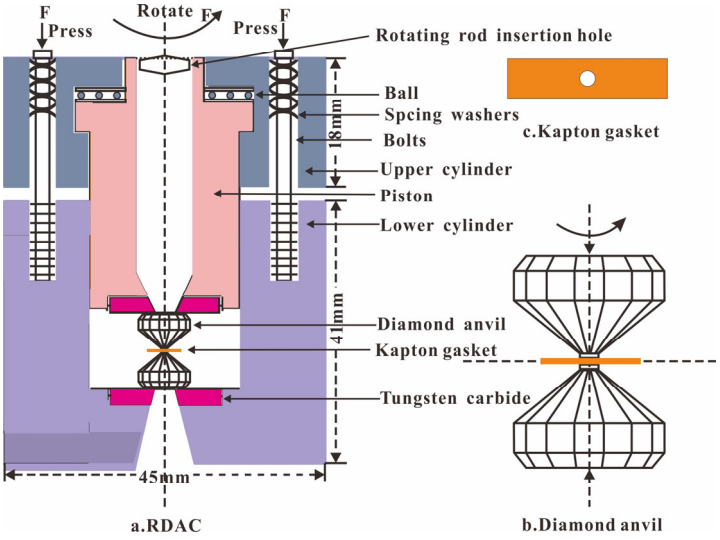


Figure 1. Rotational diamond anvil cell and the compression and shear loadings.

The stress state of the loaded diamond anvils was calibrated by diamond anvil Raman spectroscopy [17]. The calculation formula is the following function:

$$P = A\frac{\Delta\omega}{\omega_0}\left[1 + \frac{1}{2}(B-1)\frac{\Delta\omega}{\omega_0}\right]$$

where $\Delta\omega/\omega_0$ is the relative Raman frequency change of the diamond, A and B are 547 GPa and 3.75, and ω_0 = 1334 cm^{-1} is the edge frequency of the diamond.

3. Results and Discussion

3.1. The Compression and Shear Loadings Experiment with T301 Stainless Steel Gasket

3.1.1. Raman Spectroscopy of the Sample

Figure 2 shows the representative Raman spectra of antigorite in the low wavenumber region (100–1200 cm^{-1}) in the experiment with T301 stainless steel as the gasket material. The Raman spectrum at 0.1 MPa presents six observed peaks at 228, 375, 458, 635, 683, and 1045 cm^{-1}. 228 cm^{-1} that are attributed to the vibrations of the O-H-O groups and/or metal–oxygen vibrations. A measurement of 375 cm^{-1} is assigned to the bending vibrations of the SiO_4 tetrahedron. A measurement of 635 cm^{-1} corresponds to the antisymmetric OH-Mg-OH translation modes. Measurements of 683 and 1045 cm^{-1} are caused by the antisymmetric and symmetric stretching modes of Si-O_b-Si linkages. A measurement of 458 cm^{-1} was not found in the reported antigorite but in the chrysotile, which was assigned as the $\nu_3(a_1)$ mode of SiO_4 [13,18]. By increasing the axial compression stress, all these observed Raman wavenumbers shift towards higher wavenumbers, and their relative intensity remains to be resolved. When loading the shear stress at 5.0 and 8.0 GPa, there are no obvious changes for all of the Raman peaks, except for a whole movement toward high wavenumbers. When compression and shear stress are released, the recovered sample has a similar spectrum to the original sample, although its Raman peaks present at higher wavenumbers of 233, 379, 462, 640, 688, and 1051 cm^{-1}. These results indicate that antigorite's structural phase transition and amorphization do not occur in our experimental compression and shear stress region. These results agree with previous Raman studies of antigorite up to 10 GPa or 27 GPa at room temperature [10,11].

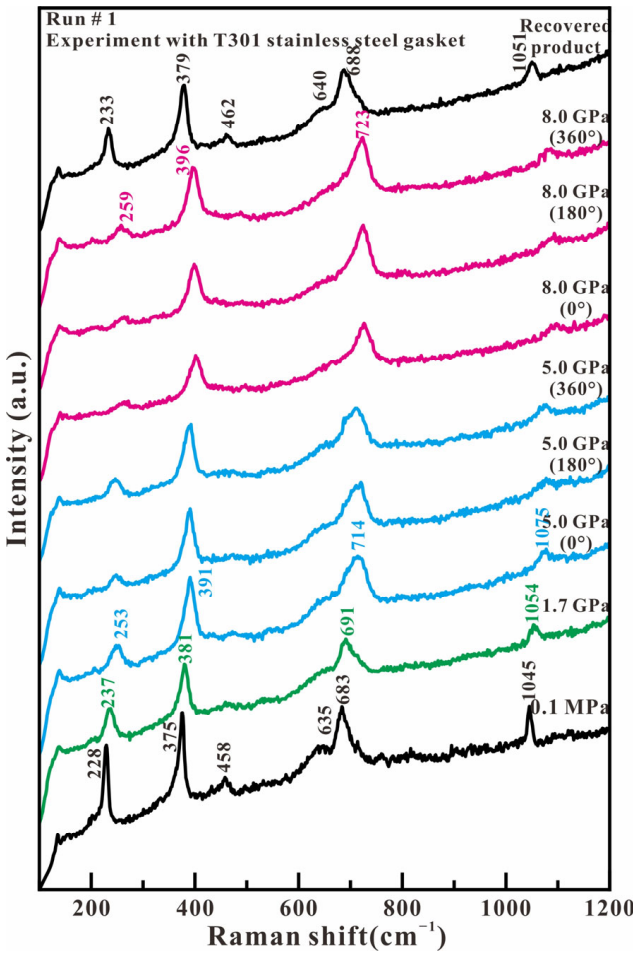


Figure 2. Representative Raman spectra of antigorite with T301 gasket in the range of 100–1200 cm^{-1} under compression and shear loading.

Figure 3 shows the representative Raman spectra of antigorite in the high wavenumber region (2750–5000 cm^{-1}) in the experiment with T301 stainless steel as the gasket material. At ambient pressure, two intense peaks at 3668 and 3699 cm^{-1} are observed, corresponding to the in-phase outer OH stretching mode and the inner OH stretching mode of antigorite, respectively. With the loading of compression and stress, there are three main changes. First, is the relative intensity reversal between the 3668 and 3699 cm^{-1} peaks. Secondly, the two intense OH stretching peaks shift simultaneously towards higher wavenumbers, but the peak 3668 cm^{-1} moves faster than the peak 3699 cm^{-1}. The third change is the appearance of two broad peaks at 3286 and 3553 cm^{-1}, which are assigned to the hydrogen-bonded OH stretch of H_2O [19–21] and the nonhydrogen-bonded OH group of H–$O^{-}\cdots$H–O–H anion $H_3O_2^{-}$ [22], respectively. With the release of compression and stress, the recovered sample not only maintains its original OH stretch peaks of antigorite at 3670 and 3700 cm^{-1}, but also has two additional OH stretching peaks of H_2O and $H_3O_2^{-}$ at 3303 and 3553 cm^{-1}, respectively. The relative intensity of the OH band in H_2O, $H_3O_2^{-}$, and antigorite indicates that only some antigorite dehydrates to form the H_2O and $H_3O_2^{-}$ under the compression and shear loadings.

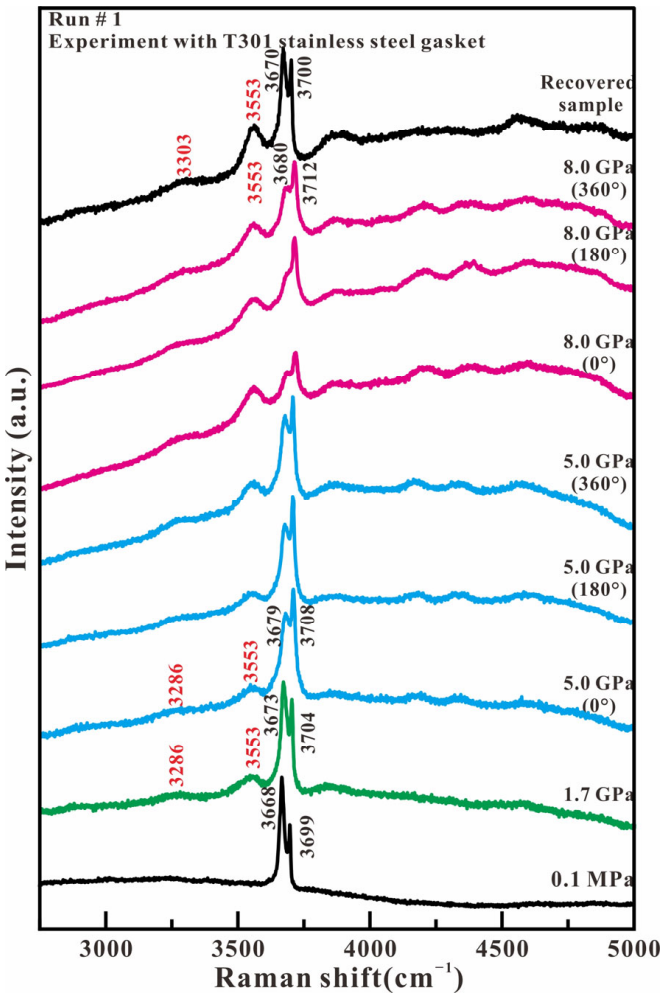


Figure 3. Representative Raman spectra of antigorite with T301 gasket in the range of 2750–5000 cm^{-1} under compression and shear loading.

The above investigation of Raman spectra in antigorite reveals that the silicon–oxygen tetrahedron SiO_4 and silicon–oxygen bridge bond Si-O_b-Si are not broken, and that only a small number of $MgO_2(OH)_4$ octahedra dehydrate under compression and shear loadings.

3.1.2. Pressure Distribution in the Chamber with the T301 Gasket

Figure 4 shows the dependence of shear stress on the rotation angle in the chamber at the central pressure up to 5.0 GPa (Figure 4a) and 8.0 GPa (Figure 4b). In the shear experiment at 5.0 GPa (Figure 4a), the shear stress exhibits a whole decrease with the rotation of the RDAC. Its maximum pressure decreases from 5.8 GPa at 0° to 5.1 GPa at 360°, and its minimum pressure decreases from 4.3 GPa at 0° to 3.1 GPa at 360°. The stress difference ($\Delta P = P_{max} - P_{min}$) shows a very small increasing trend from 1.5 GPa at 0° to 2.0 GPa at 360°. In the shear experiment at 8.0 GPa (Figure 4b), the shear stress remains wholly unchanged. The maximum pressure remains at about 9.0 GPa from 0° to 360°, and the minimum pressure remains at about 6.5 GPa from 0° to 360°. The stress difference ($\Delta P = P_{max} - P_{min}$) is about 2.5 GPa. The shear effects at 5.0 GPa and 8.0 GPa reveal that the rotation does not further affect the structural stability of antigorite even as the axial compression stress reaches 8.0 GPa.

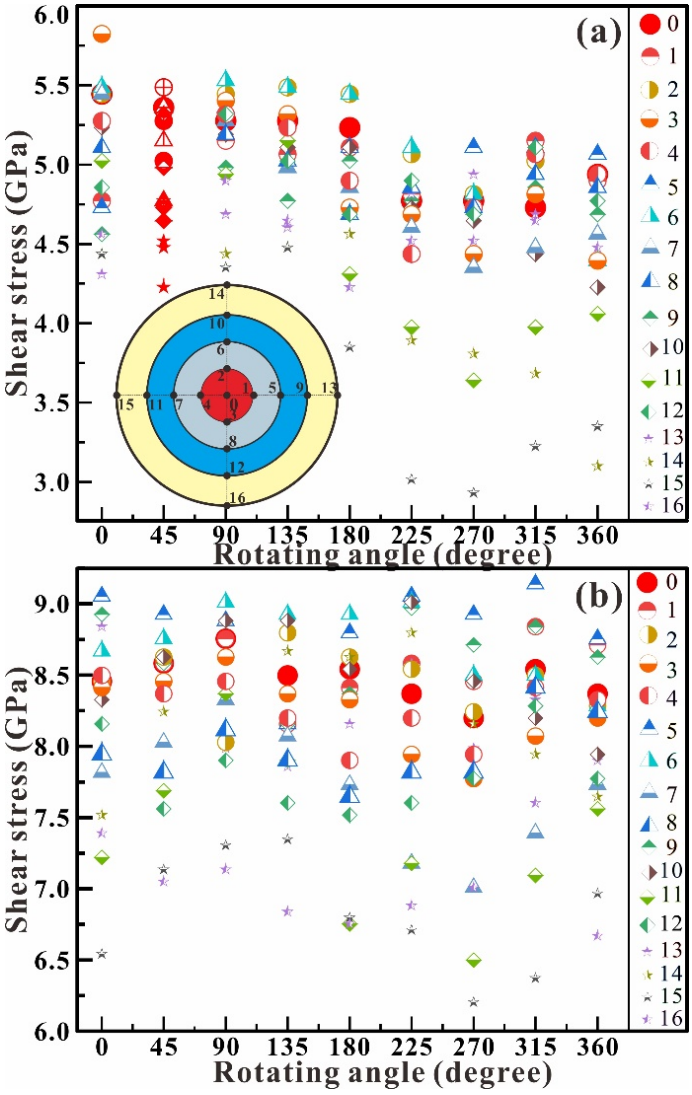


Figure 4. Dependence of shear stress on the rotation angle in the chamber at the central pressure of 5.0 (**a**) and 8.0 GPa (**b**). The insert is the distribution of the measurement points.

3.2. The Compression and Shear Loading Experiment with Kapton Plastic Gasket

3.2.1. Raman Spectroscopy of the Sample

Figure 5 shows the representative Raman spectra of antigorite in the low wavenumber region (100–1200 cm^{-1}) in the Kapton gasket experiment. The Raman spectrum at 0.1 MPa presents six observed peaks at 228, 375, 458, 635, 683, and 1045 cm^{-1}, which indicates the sample is pure antigorite. When the compression and shear stress is increased, all of these Raman peaks quickly broaden and reduce their intensity. The 228, 458, and 635 cm^{-1} peaks completely disappear at 3.0 GPa. The 1045 cm^{-1} peak completely vanishes at 3.0 GPa and 180° rotation. Finally, only the 375 and 683 cm^{-1} peaks maintain at our highest experimental pressure of 4.5 GPa. These two peaks show a positive shift towards higher wavenumbers with increased axial compression stress and compression–shear stress. Only the 379 and 681 cm^{-1} peaks are observed in the recovered sample when compression and shear stress are released. The Raman spectrum of low wavenumbers indicates that the $MgO_2(OH)_4$ octahedron has been broken under the compression of the SiO_4 tetrahedron and the Si-O_b-Si linkage under lower axial pressure and larger shear stress.

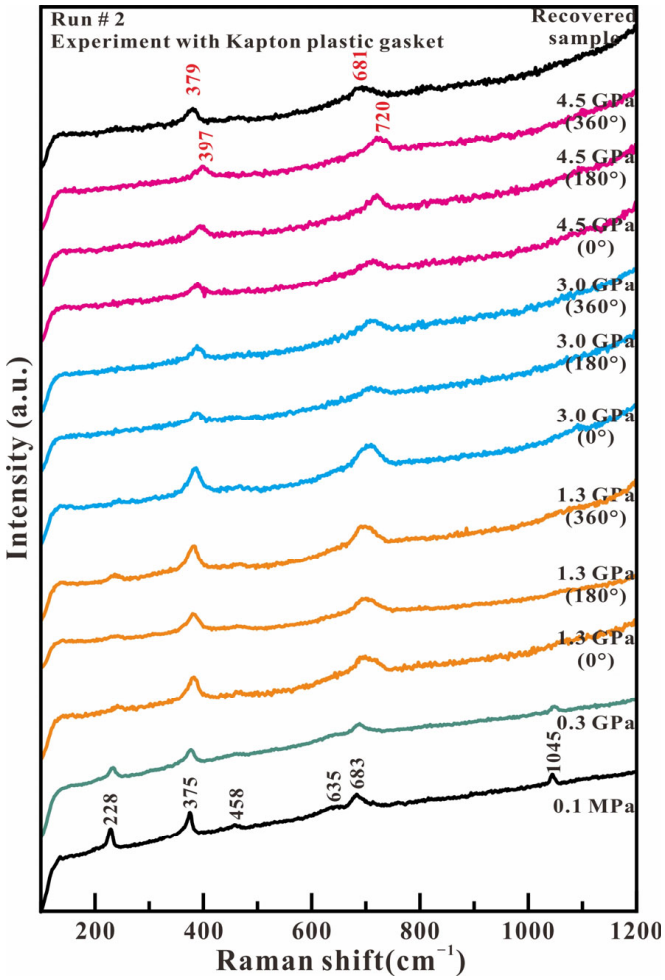


Figure 5. Representative Raman spectra of antigorite with Kapton plastic gasket in the range of 100–1200 cm^{-1} under compression and shear loading.

Figure 6 shows the representative Raman spectra of antigorite in the high wavenumber region (2750–5000 cm^{-1}) in the experiment with Kapton plastic as the gasket material. At ambient pressure, the in-phase outer OH stretching mode and the inner OH stretching mode of antigorite are observed at 3668 and 3699 cm^{-1}, respectively. With the loading of compression and stress, the relative intensity between 3668 and 3699 cm^{-1} starts to reverse at 1.3 GPa, as in the experiment with the T301 gasket. The intensity of both peaks

at 3668 and 3699 cm^{-1} rapidly reduce and completely vanish at 4.5 GPa. At 0.3 GPa, two broad peaks appear at 3303 and 3553 cm^{-1}, which are assigned to the hydrogen-bonded OH stretch of H_2O and the nonhydrogen-bonded OH group of $H–O^{-}\cdots H–O–H$ anion $H_3O_2^{-}$, respectively. The new two broad peaks shift towards a higher wavenumber and maintain their high intensity with increased axial pressure and compression–shear stress. When compression and stress is released, the recovered sample only maintains two additional OH stretching peaks of H_2O and $H_3O_2^{-}$ at 3303 and 3553 cm^{-1}. In contrast, the original OH stretching peaks of antigorite at 3668 and 3699 cm^{-1} completely disappear. The Raman spectrum of high wavenumbers indicates that the Mg $O_2(OH)_4$ octahedron breaks completely under lower axial pressure and larger shear stress. In addition, the peaks of ruby fluorescence are observed at around 4362 and 4392 cm^{-1} with a wavenumber difference of 30 cm^{-1}, and two new broad peaks appearing in the range of 3750–5000 cm^{-1}.

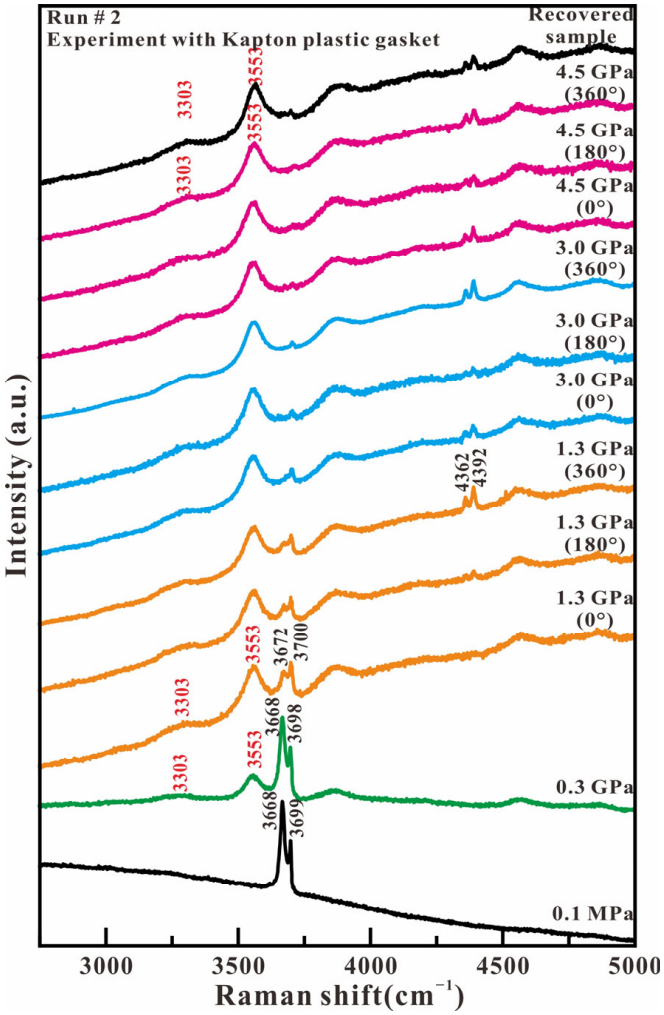


Figure 6. Representative Raman spectra of antigorite with Kapton plastic gasket in the range of 2750–5000 cm^{-1} under compression and shear loading.

3.2.2. Pressure Distribution in the Chamber with Kapton Plastic Gasket

Figure 7 shows the dependence of shear stress on the rotation angle in the chamber at typical central pressures of up to 1.3 (Figure 7a) and 3.0 GPa (Figure 7b). The shear stress remains wholly unchanged in the shear experiment at 1.3 GPa (Figure 7a). The maximum pressure remains at about 2.0 GPa from 0° to 360°, and the minimum pressure remains at about 0.5 GPa from 0° to 360°, while the stress difference ($\Delta P = P_{max} - P_{min}$) is about 1.5 GPa. In the shear experiment at 3.0 GPa (Figure 7b), the shear stress shows a significant upward trend with the increase of the rotation angle. The maximum pressure increases

from 3.7 GPa at 0° to 5.5 GPa at 360°, and the minimum pressure decreases from 1.2 GPa at 0° to 0.7 GPa at 360°. The stress difference ($\Delta P = P_{max} - P_{min}$) shows an increasing trend from 2.5 GPa at 0° to 4.8 GPa at 360°. Compared with the shear stress at 1.3 GPa and 3.0 GPa, the rotation of RDAC intensively increases the axial compression and affects the distribution of shear stress in the chamber.

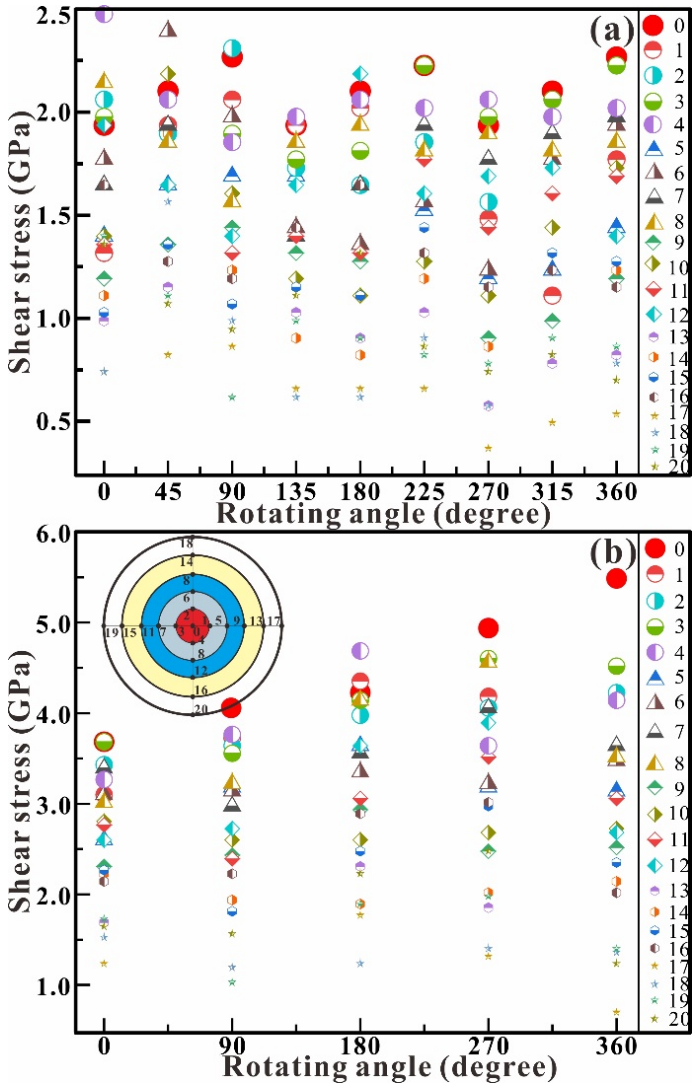


Figure 7. Dependence of shear stress on the rotation angle in the chamber at the central pressures of 1.3 (**a**) and 3.0 GPa (**b**). The inset is the distribution of the measurement points.

3.2.3. The Micro-Beam X-ray Diffraction Spectrum of the Sample

Figure 8 shows the micro-beam X-ray diffraction of antigorite before and after loading the compression and shear stress. The diffraction spectrum of the original sample shows five sharp diffraction peaks, which can be denoted as the monoclinic structure of $Mg_3(Si_2O_5)(OH)_4$ (SG: C2/m). The lattice parameters are a = 5.424 Å, b = 9.238 Å, c = 7.274 Å, and β = 91.32°, which is consistent with the reported monoclinic phase of antigorite [8]. The recovered sample from the experiment with the Kapton plastic gasket includes five observed diffraction peaks with d-spacings of 3.6210, 2.5089, 2.4236, 2.1549, and 2.8195 Å. The peak of d = 3.6210 Å is the only and strongest diffraction peak, and has the same value as the antigorite phase's (20-2) reflection. This result indicates that the layered structure of the antigorite was broken.

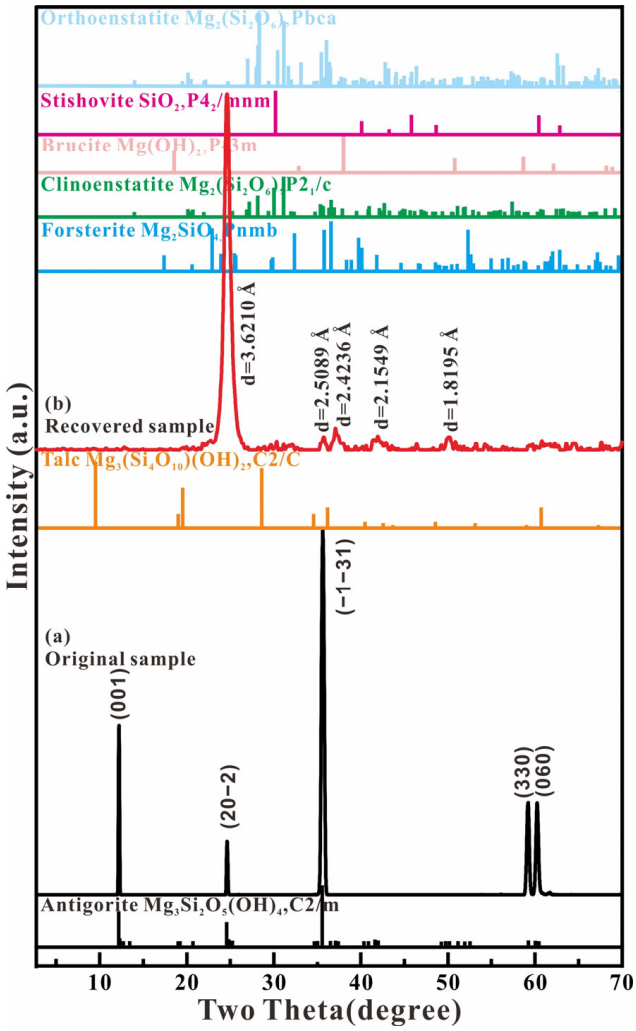


Figure 8. X-ray diffraction spectra of the starting material and recovered product and the structure index.

In order to verify the structure of the recovered product, the diffraction spectrum of the recovered sample was compared with the spectra of the dehydrated products of antigorite, such as talc $Mg_3(Si_4O_{10})(OH)_2$ (C2/c) [23], forsterite Mg_2SiO_4 (Pnmb) [24], clinoenstatite $Mg_2(Si_2O_6)$ ($P2_1/c$) [25], brucite $Mg(OH)_2$ (P-3m) [26], orthoenstatite $Mg_2(Si_2O_6)$ (Pbca) [27], and stishovite quartz SiO_2 ($P4_2/mnm$) [28]. The results show great differences in the position of the strongest peak and the pattern of the diffraction spectrum between the recovered sample and the reported dehydrated products of antigorite. Therefore, the dehydration reaction of antigorite does not form the thermodynamic stability phases. The fractured products in the Kapton plastic chamber include the sheet of rigid SiO_4 tetrahedra, the production of which is demonstrated by the Raman data. Due to the hydrogen atom's very weak X-ray diffraction effect, we cannot analyze the separation of the small molecules from the $MgO_2(OH)_4$ octahedral framework according to the conventional X-ray diffraction data.

In order to discuss the strain effect on mineral dehydration, we need to compare the material elastic moduli of the T301 stainless steel, Kapton plastic, and the sample of antigorite and analyze the accumulated plastic strain in the sample chambers. According to the references, the elastic moduli of the T301 stainless steel, antigorite, and Kapton plastic have a difference of one order of magnitude: for T301 stainless steel, the elastic modulus is E_0 = 260 GPa [29]; for antigorite, E_0 = 60.8 GPa [30,31]; and for Kapton plastic, E_0 = 5.9 GPa [32]. A strong gasket primarily suffers from stress, effectively impeding the flow of the sample to the periphery, reducing the plastic deformation and pressure

gradient in the sample. In contrast, with a weak gasket, the sample primarily suffers from compression and shear stress, further promoting the flow of the sample from the center to the periphery, finally enhancing the plastic deformation and pressure gradient in the sample.

4. Conclusions

Compression–shear stress experiments were conducted in antigorite at room temperature with different strength gasket materials. Antigorite dehydration was observed in the chamber of Kapton plastic with a lower axial compression stress and a larger gradient of shear stress. However, the antigorite in the chamber of the T301 stainless steel still maintained its layered structure with very small amounts of free fluid. The in-situ high-pressure Raman spectroscopy and ex-situ X-ray diffraction spectrum confirm that the fluid is H_2O and $H_3O_2^-$ with the OH^- stretching vibrations at 3303 and 3553 cm^{-1}, and the fractured products of rigid SiO_4 tetrahedra sheets with d-spacing at 3.6210 Å, which is about half of the original *c*-axis. Therefore, this investigation indicates that the water-bearing silicate minerals have strong shear dehydration in the cold subduction zone of the plate, which has important applications in predicting the subduction zone's physical and chemical properties and deducing the rate of plate subduction.

Author Contributions: D.T. and W.X. designed the research; D.T. and C.J. performed the research; D.T., C.J., W.C. and Y.T. analyzed the data; and D.T., C.J. and B.Y. wrote the paper. All authors have read and agreed to the published version of the manuscript.

Funding: This research was funded by the National Natural Science Foundation of China (Grants Nos. 41372047, 42172046 and 12004014) and the Strategic Priority Research Program (B) of the Chinese Academy of Sciences (XDB18010403 and XDB18010405).

Data Availability Statement: Not applicable.

Acknowledgments: We are grateful to Tongbin Shao from GIGCAS in Guangzhou for providing the natural antigorite sample and Lingya Ma from GIGCAS in Guangzhou for X-ray diffraction measurements.

Conflicts of Interest: The authors declare no conflict of interest.

References

1. Schmidt, M.W.; Poli, S. Experimentally based water budgets for dehydrating slabs and consequences for arc magma generation. *Earth Planet. Sci. Lett.* **1998**, *163*, 361–379. [CrossRef]
2. Shao, T.; Zhou, Y.; Song, M.; Ma, X.; Zhang, L.; Yao, W.; Dang, J.; Li, J. Deformation of antigorite and its geological implications. *J. Geophys. Res. Solid Earth* **2021**, *126*, e2021JB021650. [CrossRef]
3. Shao, T.; Ji, S.; Kondo, Y.; Michibayashi, K.; Wang, Q.; Xu, Z.; Sun, S.; Marcotte, D.; Salisbury, M.H. Antigorite-induced seismic anisotropy and implications for deformation in subduction zones and the Tibetan Plateau. *J. Geophys. Res. Solid Earth* **2014**, *119*, 2068–2099. [CrossRef]
4. Shao, T.; Song, M.; Ma, X.; Ding, X.; Liu, S.; Zhou, Y.; Wu, J.; Wang, X.; Li, J. Potential link between antigorite dehydration and shallow intermediate-depth earthquakes in hot subduction zones. *Am. Mineral.* **2023**, *108*, 127–139. [CrossRef]
5. Mookherjee, M.; Stixrude, L. Structure and elasticity of serpentine at high-pressure. *Earth Planet. Sci. Lett.* **2009**, *279*, 11–19. [CrossRef]
6. Wicks, F.J.; O'Hanley, D.S. Chapter 5. Serpentine Minerals: Structures and Petrology. In *Hydrous Phyllosilicates*; Bailey, S.W., Ed.; De Gruyter: Berlin, Germany; Boston, MA, USA, 1988; pp. 91–168.
7. Capitani, G.; Mellini, M. The modulated crystal structure of antigorite: The m = 17 polysome. *Am. Mineral.* **2004**, *89*, 147–158. [CrossRef]
8. Capitani, G.C.; Mellini, M. The crystal structure of a second antigorite polysome (m = 16), by single-crystal synchrotron diffraction. *Am. Mineral.* **2006**, *91*, 394–399. [CrossRef]
9. Hilairet, N.; Daniel, I.; Reynard, B. Equation of state of antigorite, stability field of serpentines, and seismicity in subduction zones. *Geophys. Res. Lett.* **2006**, *33*, L02302(1–4). [CrossRef]
10. Auzende, A.-L.; Daniel, I.; Reynard, B.; Lemaire, C.; Guyot, F. High-pressure behaviour of serpentine minerals: A Raman spectroscopic study. *Phys. Chem. Miner.* **2004**, *31*, 269–277. [CrossRef]
11. Irifune, T.; Kuroda, K.; Funamori, N.; Uchida, T.; Yagi, T.; Inoue, T.; Miyajima, N. Amorphization of serpentine at high pressure and high temperature. *Science* **1996**, *272*, 1468–1470. [CrossRef]

12. Wunder, B.; Wirth, R.; Gottschalk, M. Antigorite: Pressure and temperature dependence of polysomatism and water content. *Eur. J. Mineral.* **2001**, *13*, 485–496. [CrossRef]
13. Shen, T.; Zhang, C.; Chen, J.; Hermann, J.; Zhang, L.; Padrón-Navarta, J.A.; Chen, L.; Xu, J.; Yang, J. Changes in the cell parameters of antigorite close to its dehydration reaction at subduction zone conditions. *Am. Mineral.* **2020**, *105*, 569–582. [CrossRef]
14. Padrón-Navarta, J.A.; Hermann, J.; Garrido, C.J.; López Sánchez-Vizcaíno, V.; Gómez-Pugnaire, M.T. An experimental investigation of antigorite dehydration in natural silica-enriched serpentinite. *Contrib. Mineral. Petrol.* **2010**, *159*, 25–42. [CrossRef]
15. Ma, Y.; Selvi, E.; Levitas, V.I.; Hashemi, J. Effect of shear strain on the α–ε phase transition of iron: A new approach in the rotational diamond anvil cell. *J. Phys. Condens. Matter* **2006**, *18*, S1075. [CrossRef] [PubMed]
16. Feng, B.; Levitas, V.I. Effects of gasket on coupled plastic flow and strain-induced phase transformations under high pressure and large torsion in a rotational diamond anvil cell. *J. Appl. Phys.* **2016**, *119*, 015902. [CrossRef]
17. Akahama, Y.; Kawamura, H. Diamond anvil Raman gauge in multimegabar pressure range. *High Press. Res.* **2007**, *27*, 473–482. [CrossRef]
18. Rinaudo, C.; Gastaldi, D.; Belluso, E. Characterization of chrysotile, antigorite and lizardite by FT-Raman spectroscopy. *Can. Mineral.* **2003**, *41*, 883–890. [CrossRef]
19. Pruzan, P.; Chervin, J.; Gauthier, M. Raman spectroscopy investigation of ice VII and deuterated ice VII to 40 GPa. Disorder in ice VII. *Europhys. Lett.* **1990**, *13*, 81. [CrossRef]
20. Walrafen, G.; Abebe, M.; Mauer, F.; Block, S.; Piermarini, G.; Munro, R. Raman and x-ray investigations of ice VII to 36.0 GPa. *J. Chem. Phys.* **1982**, *77*, 2166–2174. [CrossRef]
21. Carey, D.M.; Korenowski, G.M. Measurement of the Raman spectrum of liquid water. *J. Chem. Phys.* **1998**, *108*, 2669–2675. [CrossRef]
22. Walrafen, G.E.; Douglas, R.T. Raman spectra from very concentrated aqueous NaOH and from wet and dry, solid, and anhydrous molten, LiOH, NaOH, and KOH. *J. Chem. Phys.* **2006**, *124*, 114504. [CrossRef]
23. Gruner, J.W. The crystal structures of talc and pyrophyllite. *Z. Krist.-Cryst. Mater.* **1934**, *88*, 412–419. [CrossRef]
24. Hazen, R.M. Effects of temperature and pressure on the crystal structure of forsterite. *Am. Mineral.* **1976**, *61*, 1280–1293.
25. Morimoto, N.; Appleman, D.E.; Evans, H.T., Jr. The crystal structures of clinoenstatite and pigeonite. *Z. Krist.-Cryst. Mater.* **1960**, *114*, 120–147.
26. Zhukhlistov, A.; Avilov, A.; Ferraris, D.; Zvyagin, B.; Plotnikov, V. Statistical distribution of hydrogen over three positions in the brucite $Mg(OH)_2$ structure from electron diffractometry data. *Crystallogr. Rep.* **1997**, *42*, 774–777.
27. Nestola, F.; Tribaudino, M. The structure of Pbca orthopyroxenes along the join diopside-enstatite ($CaMgSi_2O_6$-$Mg_2Si_2O_6$). *Eur. J. Mineral.* **2003**, *15*, 365–371. [CrossRef]
28. Sinclair, W.; Ringwood, A. Single crystal analysis of the structure of stishovite. *Nature* **1978**, *272*, 714–715. [CrossRef]
29. Levitas, V.; Polotnyak, S.; Idesman, A. Large elastoplastic strains and the stressed state of a deformable gasket in high pressure equipment with diamond anvils. *Strength Mater.* **1996**, *28*, 221–227. [CrossRef]
30. Bezacier, L.; Reynard, B.; Bass, J.D.; Sanchez-Valle, C.; Van de Moortèle, B. Elasticity of antigorite, seismic detection of serpentinites, and anisotropy in subduction zones. *Earth Planet. Sci. Lett.* **2010**, *289*, 198–208. [CrossRef]
31. Satta, N.; Grafulha Morales, L.F.; Criniti, G.; Kurnosov, A.; Boffa Ballaran, T.; Speziale, S.; Marquardt, K.; Capitani, G.C.; Marquardt, H. Single Crystal Elasticity of Antigorite at High Pressures and Seismic Detection of Serpentinized Slabs. *Geophys. Res. Lett.* **2022**, *49*, e2022GL099411. [CrossRef]
32. Davidson, M.; Bastian, S.; Markley, F. Measurement of the elastic modulus of Kapton perpendicular to the plane of the film at room and cryogenic temperatures. In *Supercollider 4*; Springer: Berlin/Heidelberg, Germany, 1992; pp. 1039–1045.

Disclaimer/Publisher's Note: The statements, opinions and data contained in all publications are solely those of the individual author(s) and contributor(s) and not of MDPI and/or the editor(s). MDPI and/or the editor(s) disclaim responsibility for any injury to people or property resulting from any ideas, methods, instructions or products referred to in the content.